

Study of Magnon-Photon Coupling in Ultra-thin Films Using the Derivative-Divide Method

Kang An,¹ Zhenhui Hao,¹ Yongzhang Shi,² Yingjie Zhu,¹ Xiling Li¹, Chi Zhang^{1,*} and Guozhi Chai^{1†}

¹Key Laboratory of Magnetism and Magnetic Functional Materials of the Ministry of Education, Lanzhou University, Lanzhou, 730000, People's Republic of China.

²State Key Laboratory of Crystal Materials, School of Physics, Shandong University, Jinan, 250100, People's Republic of China.

(Dated: March 12, 2026)

Magnon–photon coupling in cavity magnonic systems offers a promising route toward integrated wave-based information-processing devices. However, in ultrathin magnetic films the weak magnon response is easily buried beneath photon-dominated spectra. We show that a derivative-divide analysis of the microwave transmission parameter in a planar split-ring-resonator cavity isolates the magnetic contribution and resolves clear anticrossings in yttrium iron garnet and CoFeB films, yielding measurable coupling down to thicknesses of 60 nm and 5 nm, respectively. These results establish derivative-divide method as a simple and sensitive probe of magnon–photon coupling in ultrathin insulating and metallic films, and as a practical tool for characterizing miniaturized cavity-magnonic devices.

I. INTRODUCTION

Cavity magnonics is a rapidly developing hybrid quantum platform that investigates magnon–photon coupling (MPC)[1–4]. In such systems, the hybrid excitations—cavity magnon polaritons—possess high tunability, low energy consumption, and fast response, making them promising candidates for high-performance reservoir computing devices [5, 6]. Yttrium iron garnet (YIG) is widely used in cavity magnonics to provide magnon modes, owing to its low magnetic damping[7, 8]. Placing a YIG sample in a three-dimensional microwave cavity enables efficient information exchange between magnons and photons[9–21]. However, practical on-chip integration requires miniaturizing MPC platforms. In this regard, planar resonators are particularly attractive because their smaller mode volume, compared with three-dimensional cavities, facilitates compact device implementations [22–28].

Planar resonators are compact and readily compatible with integrated circuits, offering broad application prospects. When YIG spheres are placed on planar resonators, several notable phenomena emerge. Breaking system symmetries in non-Hermitian settings enables nonreciprocal coupling [23, 24, 26, 29, 30]. Positioning the YIG sphere within a cross cavity provides spatial control of MPC[31, 32]. Rao *et al.* positioned a YIG sphere atop a coplanar waveguide, realizing coupling to ferrimagnetic Walker modes and meterscale strong coupling between magnons and photons [25, 33]. Beyond spheres, YIG films provide a large contact area with planar resonators and are better suited for integrated-device development. Huebl *et al.* first demonstrated MPC using Ga-doped YIG films coupled to a superconducting

resonator at millikelvin temperatures [34]. Bai *et al.* employed a YIG/Pt bilayer to coherently manipulate pure spin currents by combining spin pumping with MPC [35]. Shi *et al.* tuned MPC by varying the split-ring resonator (SRR) width, thereby modulating the microwave magnetic field acting on the YIG film [36]. Kim *et al.* observed a pronounced negative refractive index arising from non-Hermitian properties in a YIG film coupled to an inverted SRR [27]. Xiong *et al.* introduced a microwave metaresonator combining split-ring and spiral resonators, achieving more than an order-of-magnitude enhancement of photon–magnon coupling [37]. Ongoing studies using YIG films [22, 28, 38–42] and other magnetic films [43–45] continue to probe magnon–photon interactions. These films typically have micrometer-scale thickness. Further reducing the thickness eases control of anisotropy and dispersion and also reduces cost and fabrication time, which is beneficial for integrated-circuit applications.

However, reducing thickness also lowers the total magnetic moment. Consequently, magnon signatures weaken relative to photon modes. In conventional transmission measurements, cavity photon modes can dominate the spectrum, so that the magnon mode and the associated MPC signatures may evade detection. To overcome this limitation and reveal these interactions, we adopt the derivative-divide method [46] as a sensitive probe of MPC. We first perform comparative measurements on conventional YIG systems to show that this method reliably resolves MPC in a magnon-dominated regime. We then study YIG films of varying thickness and detect resonator-mediated MPC even in the thinnest sample (60 nm). Furthermore, for high-damping magnetic films, coupling to photon modes is still observed. Measurements on CoFeB (CFB) films yield an apparently stronger effective coupling strength. Finally, by comparing CFB thicknesses across experiments, we demonstrate a breakthrough in testing capability for ultra-thin films. Our results provide a practical pathway for MPC

* Correspondence email address: zc@lzu.edu.cn

† Correspondence email address: chaigzh@lzu.edu.cn

studies in magnetic thin films and may facilitate future magnon–photon device development.

II. EXPERIMENTS AND METHODS

The experimental system consists of a vector network analyzer (VNA), SRR, magnetic samples, and an electromagnet. As shown in Fig. 1(a), the SRR is fabricated by optical lithography on a dielectric substrate with a relative permittivity of 3.55. The thicknesses of the SRR, the microstrip line, and the grounding plate are all $35\ \mu\text{m}$, while the thickness of the dielectric substrate is $0.778\ \text{mm}$. The geometrical parameters of the SRR and the microstrip line are also indicated in Fig. 1(a): $a = 10\ \text{mm}$, $g = 0.3\ \text{mm}$, $w_1 = 1.68\ \text{mm}$, and $w_2 = 0.65\ \text{mm}$. In our design, the bare SRR supports three resonance modes at $2.59\ \text{GHz}$, $4.98\ \text{GHz}$, and $7.71\ \text{GHz}$, as shown in Fig. 2(a).

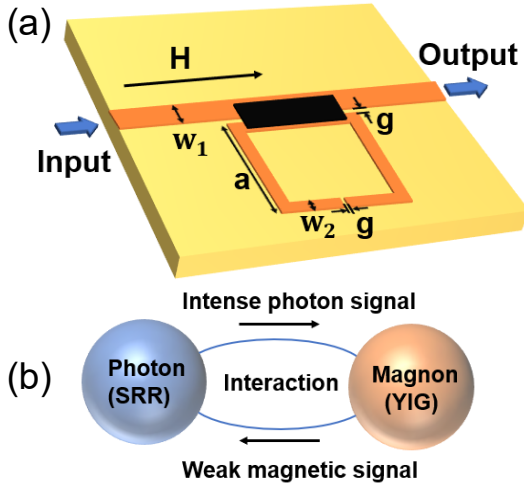


FIG. 1. (a) Sketch of the split-ring resonator structure, showing the placement of the magnetic samples (black rectangle). Microwave signals are input from the input terminal and output from the output terminal. The applied magnetic field is parallel to the microstrip line. (b) Schematic of the interaction between photon and magnon.

For the magnetic samples, we use both YIG and CFB films. The YIG films, which are used for comparison testing, are grown by pulsed laser deposition (PLD) on gadolinium gallium garnet (GGG) substrates. To investigate thickness-dependent behavior, we prepare YIG films with several different thicknesses. The CFB films, used for extended testing, are deposited by magnetron sputtering on silicon substrates. We first measure the S-parameters directly for all samples and then perform comparative measurements on the thinner films using the differential method. An in-plane magnetic field is applied parallel to the microstrip line by means of an electromagnet.

To enhance the sensitivity to MPC, we apply a new test method, the derivative-divide technique. In a typical

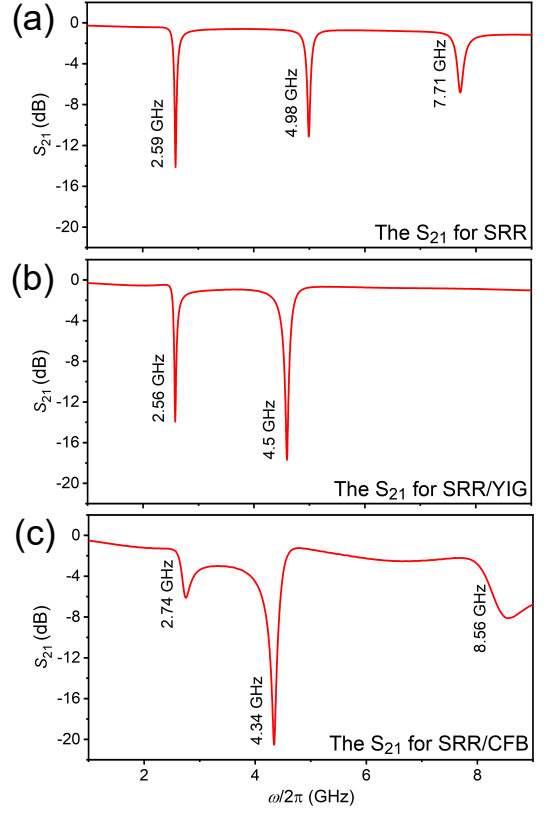


FIG. 2. (a)-(c) In a zero magnetic field, the S_{21} plot for the SRR, the SRR with a YIG film and the SRR with a CFB film.

MPC measurement using a VNA, the microwave transmission parameter S_{21} is measured as a function of frequency under a series of applied magnetic fields (H_0). The parameter S_{21} is defined as the ratio of the output voltage (V_o) to the input voltage (V_i), and can be written as $S_{21} = V_o/V_i \cdot e^{i\phi}$, where ϕ is the phase delay. When the magnetic sample is placed at a certain position on the resonator, the induced voltage at that location can be expressed in terms of $\chi(\omega, H_0)$ [47]

$$V_{inductive} = -i\omega A e^{i\phi} V_o \chi(\omega, H_0). \quad (1)$$

Here, A is a real-valued scaling parameter, and $\chi(\omega, H_0)$ is the magnetic permeability at frequency ω and magnetic field H_0 . Due to transmission losses and the electrical length of the microwave setup, S_{21} can therefore be parameterized as:

$$S_{21} = \frac{-i\omega A V_o \chi(\omega, H_0) + V_o^{BG}(\omega)}{V_i} e^{i\phi}. \quad (2)$$

We performed differentiation on S_{21} under different magnetic fields:

$$d_D S_{21} = \frac{S_{21}(\omega, H_0 + \Delta H) - S_{21}(\omega, H_0 - \Delta H)}{S_{21}(\omega, H_0) \Delta H}. \quad (3)$$

Expanding and reducing the terms in Eq. 3 yields:

$$\begin{aligned} d_D S_{21} &\approx -i\omega A \frac{\chi(\omega, H_0 + \Delta H) - \chi(\omega, H_0 - \Delta H)}{\Delta H} \\ &= -i\omega A' \frac{d\chi}{d\omega}. \end{aligned} \quad (4)$$

Here, A' is a constant, defined as $A' = A \frac{d\omega}{dH_0}$. First, we calculated $d_D S_{21}$ using the measured S_{21} , then divided it by the frequency ω to obtain the rate of change of magnetic susceptibility:

$$-iA' \frac{d\chi}{d\omega} = \frac{S_{21}(\omega, H_0 + \Delta H) - S_{21}(\omega, H_0 - \Delta H)}{\omega S_{21}(\omega, H_0) \Delta H}. \quad (5)$$

Using the new test method (derivative divide), we can eliminate the effects of microwave setup. The real part was taken for plotting.

III. RESULTS AND DISCUSSION

A. Experiments of YIG

As shown in Fig. 1(b), in the planar cavity–magnetic-film system the magnon signal is weak, whereas the photon signal is strong. In such a photon-dominated situation, the influence of the cavity photons on the magnons is pronounced, but the magnon contribution to the transmission spectrum is easily masked; by contrast, MPC is more readily observed in magnon-dominated systems. When a YIG film is placed on the SRR, the resonance modes appear at 2.56 GHz and 4.5 GHz, as shown in Fig. 2(b).

To make a direct comparison with conventional measurements, we first test the 100 nm YIG film using two distinct methods—standard S_{21} transmission measurements and the derivative-divide method—the results of which are shown in Fig. 3(a) and 3(b), respectively. Figure 3(a) shows the microwave transmission parameter S_{21} measured as a function of frequency ($\omega/2\pi$) under varying magnetic fields (H). In this case, only the photon modes of the SRR are visible, while both the ferromagnetic resonance (FMR) of YIG and the signatures of MPC remain invisible. Based on the measurement results in Fig. 3(b), we zoomed in on the coupling region between magnon and photon modes to observe the MPC. It can be seen that only the photon mode with narrow linewidth exhibit very weak interaction, while no interaction is observable in photon modes with large linewidths. This is because the photon signal from the SRR is significantly stronger than the magnetic signal from the YIG film. Consequently, even within the anticipated MPC regime, the influence of the magnetic response on the photon modes is negligible. In contrast, the result in Fig. 3(b) is obtained using the derivative-divide method, which is specifically designed to enhance the magnetic

contribution. By processing the data in terms of changes in magnetic permeability, this method clearly reveals the FMR of YIG and the associated MPC. The effective removal of background interference allows for precise extraction of magnetic parameters, such as the resonance frequency and linewidth.

In the coupling region, the MPC is clearly resolved in the derivative-divide spectra. Here, the strong photon field of the SRR exerts a significant influence on the weak magnetic resonance signal of the YIG film, manifesting as a splitting of the FMR peak into two distinct hybridized modes. This behavior is analyzed at 2.56 GHz and 4.5 GHz in Fig. 3(c) and 3(d), respectively. In this paper, we employ a color-coded representation for the derivative parameter $d_D S_{21}$. Red regions indicate where $d_D S_{21}$ is negative, corresponding to a positive rate of change in magnetic permeability. Conversely, blue regions indicate where $d_D S_{21}$ is positive, corresponding to a negative rate of change. The white boundary between the red and blue regions signifies $\frac{d\chi}{d\omega} = 0$, which aligns precisely with the FMR frequency for each magnetic field. This boundary serves as a critical reference for fitting the FMR and the MPC. The variation in the rate of change of magnetic permeability within the coupling region also aids in distinguishing the upper and lower coupling branches. The coupling strength κ_q is quantitatively extracted by fitting the experimental data to the following formula [48]

$$\omega_{\pm} = \frac{1}{2}(\omega_c + \omega_m) \pm \frac{1}{2}\sqrt{(\omega_c - \omega_m)^2 + 4\kappa_q^2}, \quad (6)$$

where ω_{\pm} are the frequencies of the coupled resonances, while ω_c and ω_m denote the uncoupled resonance frequencies of the SRR and the YIG film, respectively. At the center of the anti-crossing region, the coupling strength simplifies to $\kappa_q = \frac{|\omega_+ - \omega_-|}{2}$, where $|\omega_+ - \omega_-|$ represents the frequency splitting between the two hybridized modes. Fitting the experimental data yields coupling strengths of 50 MHz and 54 MHz at 2.56 GHz and 4.5 GHz, respectively. These results confirm that magnetic-signal characterization via the derivative-divide method effectively captures MPC dynamics.

Having validated the method on the 100 nm film, we next test thinner YIG samples (80 nm and 60 nm) alongside the 100 nm sample for comparison. Fitting the data using Eq. 6 yields coupling strengths κ_q of 50 MHz, 47 MHz, and 40 MHz for the 100 nm, 80 nm, and 60 nm films, respectively. These experimental results demonstrate that the MPC strength decreases as the film thickness is reduced, although the variation is relatively small, which can be attributed to the approximately constant photon number in the cavity. The proposed test method thus successfully enables the measurement of coupling between ultra-thin magnetic films and cavity photon modes, thereby facilitating the systematic study of thin-film-based magnetic samples.

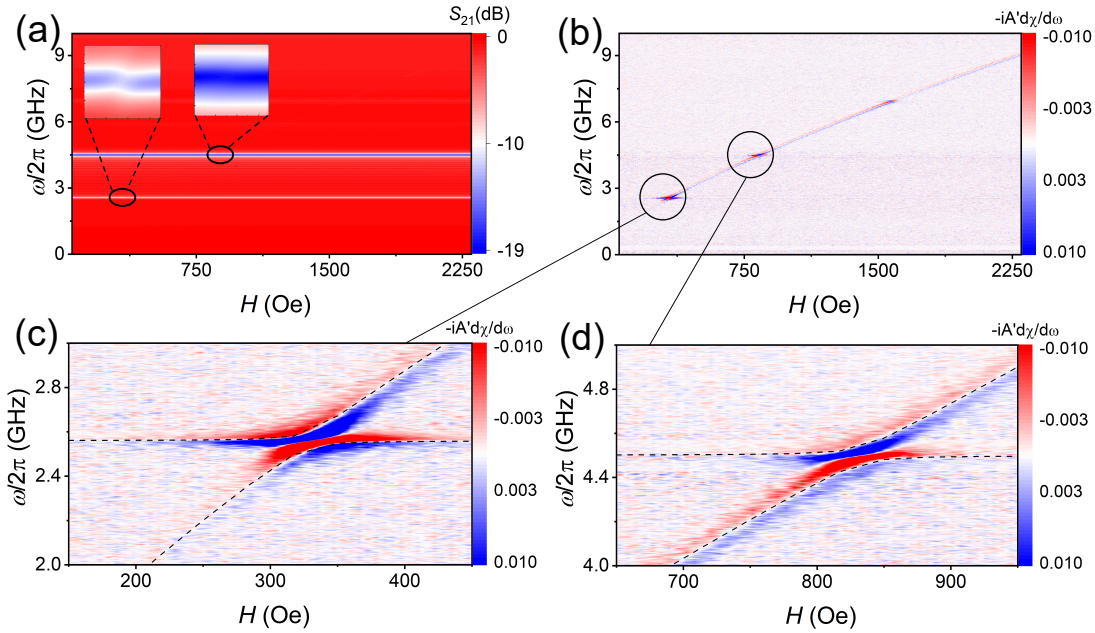


FIG. 3. Comparative testing of 100 nm YIG film. (a) Mapping of the amplitude of the transmission coefficient S_{21} as a function of frequency and applied static magnetic field. The coupling region is displayed with magnification in the figure. (b) Mapping of the rate of change of magnetic permeability as a function of frequency and applied static magnetic field. (c) and (d) The coupling of the magnon and photon modes, with the coupling strengths fitted by Eq. 6, is 50 MHz and 54 MHz, respectively.

B. Experiments of CoFeB

We demonstrate that the derivative-divide method not only measures the coupling between non-metallic thin-film samples and photon modes, but is also applicable to metallic films. Using the setup shown in Fig. 1(a), we replace the YIG samples with CFB samples and characterize films with thicknesses of 114.65 nm, 15.92 nm, and 5 nm. When a CFB film is placed on the SRR, the resonance modes appear at 2.74 GHz, 4.34 GHz, and 8.56 GHz, as shown in Fig. 2(c). Among these, we select the photon mode at 8.56 GHz for MPC measurements. As discussed in the Appendix, the substrate has a negligible effect on the photon modes; instead, it is the magnetic sample that affects both their frequency and linewidth. The CFB film is placed in direct contact with the SRR and the microstrip line, forming a hybrid photon-magnon system. Unlike insulating YIG, CFB is electrically conductive; this conductivity causes it to reflect and redistribute the electromagnetic field, thereby altering the transmission characteristics of the microstrip line and modifying the photon modes of the SRR [49]. Nevertheless, these modified photon modes still couple to the FMR of CFB, enabling direct measurement of MPC.

Figure 4 shows the coupling spectra between the magnon modes of the 114.65 nm, 15.92 nm, and 5 nm CFB films and the modified photon modes of the SRR, obtained using the derivative-divide method. Fitting these data with Eq. 6 yields coupling strengths of 350 MHz, 270 MHz, and 100 MHz, respectively. From Fig. 4, it is evident that the signal from the 114.65 nm film

is significantly stronger than those from the 15.92 nm and 5 nm films. This behavior can be attributed to the positive correlation between the detected signal and the total magnetic volume: a larger volume corresponds to a larger total magnetic moment and thus a stronger signal. In our present setup, 5 nm is the thinnest CFB film for which coupling to the SRR cavity can still be resolved; for thinner films, the coupling signal falls below the detection limit. Furthermore, a comparative analysis reveals that the CFB samples exhibit stronger signals than the YIG samples. This discrepancy originates from the higher saturation magnetization of CFB, which corresponds to a larger dynamic magnetic permeability. Consequently, the magnetic permeability of the CFB films undergoes a more rapid variation with frequency, leading to a stronger response in the derivative-divide spectra.

C. Application Prospects in Integrated Devices

In next-generation information processing, magnons are poised to serve as key information carriers. To effectively control magnon transport, the design of magnetic devices has long attracted significant attention. As a fundamental building block in magnonics, the magnon transistor already has well-established design approaches [50–52]. To control magnon transport in transistors, Wang *et al.* proposed that the spin-magnon conversion efficiency can be enhanced or suppressed using a gate voltage [53]. Several other independent magnon-based computing devices have also been demonstrated to be feasible, includ-

ing spin-wave logic gates [54], spin-wave majority gates [55], and nanoscale neural networks based on non-linear spin-wave interference [56]. To realize cascaded magnon components in integrated magnon circuits, Wang *et al.* further proposed an all-magnetic repeater based on bistability to overcome spin-wave amplitude degradation and phase distortion during propagation [57].

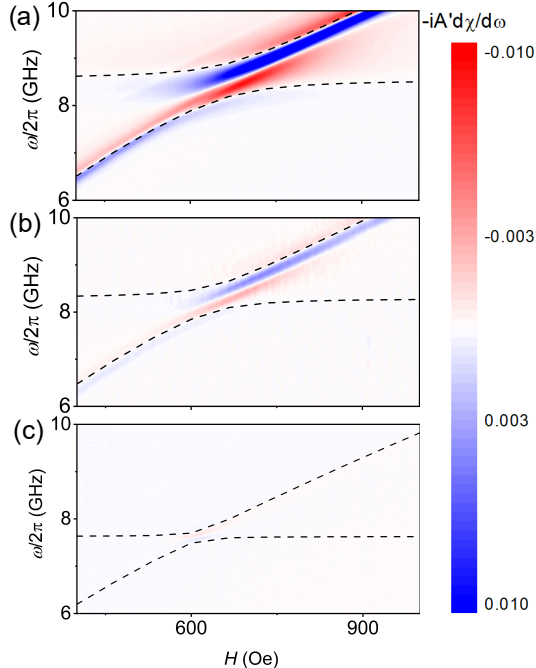


FIG. 4. (a)-(c) MPC for the 114.65 nm, 15.92 nm and 5 nm CFB samples. The measured MPC strengths, fitted using Eq. 6, are 350 MHz, 270 MHz and 100 MHz, respectively.

TABLE I. Comparison of the testing system in this work with those reported in the literature

Magnetic films	Thickness	Resonators	Reference
La:YIG	83 μm	Stripline resonator	[39]
YIG	25 μm	Inverted split-ring	[38]
YIG	25 μm	Inverted split-ring	[27]
YIG	5 μm	Metamaterial planar	[40]
YIG	4 μm	Split-ring	[36]
YIG	2 μm	Double-split-ring	[37]
YIG	60 nm	Split-ring	This work

Unlike the aforementioned magnetic devices, MPC merges concepts from quantum optics and magnetism, linking microwave photons with magnons. The resulting cavity magnon polaritons, which have the potential to carry and process information, can serve as new functional elements in integrated circuits. However, existing experimental systems typically perform coupling measurements on YIG films with thicknesses on the micrometer scale, which does not meet the requirements of device miniaturization. Our testing method directly addresses this limitation and can facilitate the development

of miniaturized magnon-photon devices. We have compared several previously reported systems for testing YIG films, and Table I summarizes the YIG film thicknesses employed in these works [27, 36–40]. It is evident that the minimum YIG film thickness accessible in our measurements is significantly smaller than those reported in previous experiments. Using the derivative-divide method, we have achieved reliable coupling measurements on YIG films with thicknesses of only several tens of nanometers. For magnetic samples with higher saturation magnetization, the rate of change of their magnetic permeability with frequency is larger, which enables the testing of even thinner films. As technology continues to advance, future MPC systems will place increasing emphasis on the miniaturization and integration of both samples and resonators. The testing method proposed in this work provides a practical route to overcoming current measurement limitations and supports the development of ultra-thin-film-based magnon-photon devices.

IV. SUMMARY

In summary, we have validated the reliability of the derivative-divide method using the YIG/SRR system, demonstrating that it can resolve MPC and reliably extract the coupling strength in a magnon-dominated regime. The generalizability of this method is further verified with the CFB/SRR system, confirming its applicability to diverse magnetic thin-film samples. By effectively suppressing extraneous background contributions, this approach isolates the magnetic response and enables quantitative analysis of key parameters such as the dispersion and damping of cavity magnon polaritons dominated by magnon modes. Using an established MPC model to fit the derivative-divide spectra, we obtain excellent agreement with experiment and extract parameters including the coupling strength. In addition, we identify critical factors that govern the signal amplitude, namely the magnetic sample volume (total magnetic moment) and the saturation magnetization. Taken together, these results show that the proposed testing framework is a powerful tool for probing the coupling between weak magnon modes and cavity photon modes, and it provides a practical route toward magnon-photon-based quantum information processing and cavity-magnonic oscillator devices.

ACKNOWLEDGEMENTS

This work is supported by the National Natural Science Foundation of China (NSFC) (Nos. 52471200, 12174165 and 52201219) and Scientific Research Innovation Capability Support Project for Young Faculty (ZYGXQNJSKYCXNLZCXM-I19).

APPENDIX A: EFFECT OF THE SUBSTRATE

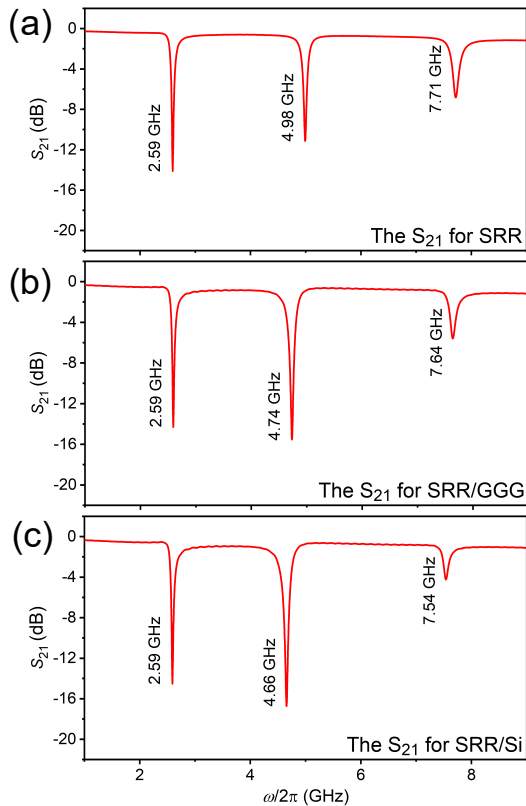


FIG. 5. (a)-(c) In a zero magnetic field, the S_{21} plot for the SRR, the SRR with GGG and the SRR with Si.

In the main text, we mention that placing the sample induces specific alterations in the photon modes of the entire system. To further clarify that these changes are caused by the magnetic material rather than the substrate, we separately placed the substrate onto the SRR to observe the variations in the photon modes.

In the absence of an applied external magnetic field, we measured the transmission parameter maps for the following configurations: the empty cavity, the SRR with a GGG substrate, and the SRR with a Si substrate, as shown in Fig. 5(a)-(c). A comparison of the photon modes across these maps indicates that the substrates induce only a minor frequency shift in the photon modes and do not substantially affect the overall system. Furthermore, in the actual experimental setup, the magnetic sample is in direct contact with the SRR, rather than with any substrate. Consequently, it can be concluded that the observed changes in the photon modes of the system are attributable to the magnetic sample.

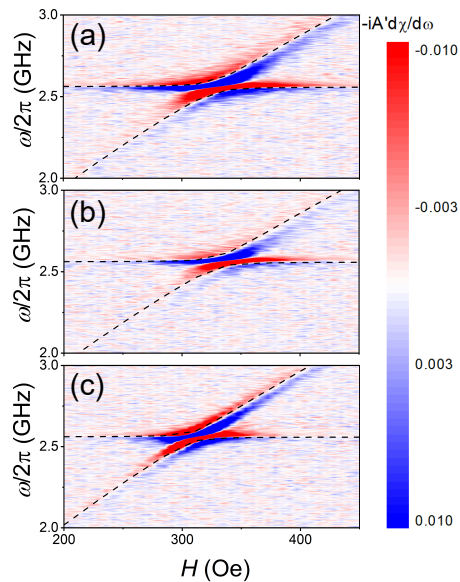


FIG. 6. Magnified view of the coupling region between 100 nm / 80 nm / 60 nm YIG and the first photon mode.

APPENDIX B: TESTS ON YIG SAMPLES OF VARYING THICKNESSES

We investigated the magnon-photon coupling of YIG films with a series of thicknesses, including 100 nm, 80 nm and 60 nm. All of these films exhibited magnon modes and their coupling with photon modes. Their spectral features appeared similar, and magnified views of the coupling regions with the first photon mode are presented in Fig. 6(a)-(c). Fitting the data using Eq. 6 yields coupling strengths κ_q of 50 MHz, 47 MHz, and 40 MHz for the 100 nm, 80 nm, and 60 nm films, respectively.

APPENDIX C: DERIVATIVE-DIVIDE

When the magnetic sample is placed at a certain position on the resonator, the induced voltage at that location can be expressed as Eq. 1. To account for influences such as energy dissipation during transmission, a correction term $V_o^{BG}(\omega)e^{i\phi}$ can be introduced. The output voltage can then be expressed in the form of $V_o = (-i\omega AV_o\chi(\omega, H_0) + V_o^{BG}(\omega))e^{i\phi}$. S_{21} is obtained by dividing the output voltage V_o by the input voltage V_i , as given in Eq. 2.

We performed the calculation using derivative-divide by taking a differential magnetic field ΔH , dividing the difference in S_{21} between the two magnetic fields by the center frequency and the differential magnetic field, as given in Eq. 3. By substituting Eq. 2 into Eq. 3, the expression can be simplified by eliminating redundant terms:

$$d_D S_{21} = \frac{-i\omega A V_o (\chi(\omega, H_0 + \Delta H) - \chi(\omega, H_0 - \Delta H))}{\Delta H (-i\omega A V_o \chi(\omega, H_0) + V_o^{BG}(\omega))}. \quad (7)$$

Since $V_o = (-i\omega A V_o \chi(\omega, H_0) + V_o^{BG}(\omega))e^{i\phi}$, Eq. 7 can be further simplified:

$$\begin{aligned} d_D S_{21} &\approx -i\omega A \frac{\chi(\omega, H_0 + \Delta H) - \chi(\omega, H_0 - \Delta H)}{\Delta H} \\ &= -i\omega A \frac{d\chi}{dH}. \end{aligned} \quad (8)$$

Within a certain frequency range, it is approximated that the resonance frequency of the magnetic sample varies linearly with the applied external magnetic field. Consequently, the dependence of magnetic susceptibility on the magnetic field can be transformed into its dependence on frequency:

$$d_D S_{21} = -i\omega A \frac{d\chi}{d\omega} \frac{d\omega}{dH_0} = -i\omega A' \frac{d\chi}{d\omega}. \quad (9)$$

-
- [1] M. Harder and C.-M. Hu, Cavity spintronics: An early review of recent progress in the study of magnon-photon level repulsion, *Solid State Phys.* **69**, 47 (2018).
- [2] B. Bhoi and S.-K. Kim, Photon-magnon coupling: Historical perspective, status, and future directions, *Solid State Phys.* **70**, 1 (2019).
- [3] C.-M. Hu, The 2020 roadmap for spin cavitronics, *Solid State Phys.* **71**, 117 (2020).
- [4] B. Zare Rameshti, S. Viola Kusminskiy, J. A. Haigh, K. Usami, D. Lachance-Quirion, Y. Nakamura, C.-M. Hu, H. X. Tang, G. E. Bauer, and Y. M. Blanter, Cavity magnonics, *Phys.Rep.* **979**, 1 (2022).
- [5] L. Millet, H. Jeon, B. Kim, B. Bhoi, and S.-K. Kim, Reservoir computing using photon-magnon coupling, *Appl. Phys. Lett.* **119**, 182405 (2021).
- [6] X. Wang, X. Mi, F. Yang, Q. Wang, L. Bai, Y. Tian, J. Rao, and S. Yan, Speech recognized by cavity magnon polaritons, *Adv. Funct. Mater.* **35**, 2500782 (2025).
- [7] V. Cherepanov, I. Kolokolov, and V. L'vov, The saga of YIG: Spectra, thermodynamics, interaction and relaxation of magnons in a complex magnet, *Phys.Rep.* **229**, 81 (1993).
- [8] A. A. Serga, A. V. Chumak, and B. Hillebrands, YIG magnonics, *J. Phys. D: Appl. Phys.* **43**, 264002 (2010).
- [9] X. Zhang, C.-L. Zou, L. Jiang, and H. X. Tang, Strongly coupled magnons and cavity microwave photons, *Phys. Rev. Lett.* **113**, 156401 (2014).
- [10] D. Zhang, X.-M. Wang, T.-F. Li, X.-Q. Luo, W. Wu, F. Nori, and J. You, Cavity quantum electrodynamics with ferromagnetic magnons in a small yttrium-iron-garnet sphere, *Npj Quantum Inf.* **1**, 15014 (2015).
- [11] X. Zhang, C.-L. Zou, N. Zhu, F. Marquardt, L. Jiang, and H. X. Tang, Magnon dark modes and gradient memory, *Nat. Commun.* **6**, 8914 (2015).
- [12] X. Zhang, C.-L. Zou, L. Jiang, and H. X. Tang, Cavity magnomechanics, *Sci. Adv.* **2**, e1501286 (2016).
- [13] D. Zhang, X.-Q. Luo, Y.-P. Wang, T.-F. Li, and J. Q. You, Observation of the exceptional point in cavity magnon-polaritons, *Nat. Commun.* **8**, 1368 (2017).
- [14] D. Lachance-Quirion, Y. Tabuchi, S. Ishino, A. Noguchi, T. Ishikawa, R. Yamazaki, and Y. Nakamura, Resolving quanta of collective spin excitations in a millimeter-sized ferromagnet, *Sci. Adv.* **3**, e1603150 (2017).
- [15] M. Harder, Y. Yang, B. M. Yao, C. H. Yu, J. W. Rao, Y. S. Gui, R. L. Stamps, and C.-M. Hu, Level attraction due to dissipative magnon-photon coupling, *Phys. Rev. Lett.* **121**, 137203 (2018).
- [16] J. Xu, C. Zhong, X. Han, D. Jin, L. Jiang, and X. Zhang, Floquet cavity electromagnonics, *Phys. Rev. Lett.* **125**, 237201 (2020).
- [17] H. Pan, Y. Yang, Z. H. An, and C.-M. Hu, Bistability in dissipatively coupled cavity magnonics, *Phys. Rev. B* **106**, 054425 (2022).
- [18] M.-X. Bi, H. Fan, X.-H. Yan, and Y.-C. Lai, Folding state within a hysteresis loop: Hidden multistability in nonlinear physical systems, *Phys. Rev. Lett.* **132**, 137201 (2024).
- [19] Y. Yang, J. Yao, Y. Xiao, P.-T. Fong, H.-K. Lau, and C.-M. Hu, Anomalous long-distance coherence in critically driven cavity magnonics, *Phys. Rev. Lett.* **132**, 206902 (2024).
- [20] C. Zhang, Z. Hao, Y. Shi, X. Li, C. Jiang, C. K. Ong, D. Gao, and G. Chai, Simultaneous realization of nonreciprocal and ultra-strong coupling in cavity magnonics, *npj Spintron.* **3**, 45 (2025).
- [21] Z. Hao, Y. Yao, K. An, X. Li, C. Zhang, and G. Chai, Selectively dissipative and coherent couplings mediated by the interaction between antiresonance and multiple magnons, *Phys. Rev. B* **112**, 064416 (2025).
- [22] B. Bhoi, T. Cliff, I. S. Maksymov, M. Kostylev, R. Aiyar, N. Venkataramani, S. Prasad, and R. L. Stamps, Study of photon-magnon coupling in a yig-film split-ring resonant system, *J.Appl. Phys.* **116**, 243906 (2014).
- [23] Y.-P. Wang, J. W. Rao, Y. Yang, P.-C. Xu, Y. S. Gui, B. M. Yao, J. Q. You, and C.-M. Hu, Nonreciprocity and unidirectional invisibility in cavity magnonics, *Phys. Rev. Lett.* **123**, 127202 (2019).
- [24] Y. Yang, Y.-P. Wang, J. W. Rao, Y. S. Gui, B. M. Yao, W. Lu, and C.-M. Hu, Unconventional singularity in anti-parity-time symmetric cavity magnonics, *Phys. Rev. Lett.* **125**, 147202 (2020).
- [25] J. W. Rao, B. Yao, C. Y. Wang, C. Zhang, T. Yu, and W. Lu, Unveiling a pump-induced magnon mode via its strong interaction with walker modes, *Phys. Rev. Lett.* **130**, 046705 (2023).
- [26] J. Qian, J. Li, S.-Y. Zhu, J. Q. You, and Y.-P. Wang, Probing pt -symmetry breaking of non-hermitian topological photonic states via strong photon-magnon coupling, *Phys. Rev. Lett.* **132**, 156901 (2024).
- [27] J. Kim, B. Kim, B. Kim, H. Jeon, and S.-K. Kim, Magnetic-field controlled on-off switchable non-reciprocal negative refractive index in non-Hermitian photon-magnon hybrid systems, *Nat. Commun.* **15**, 9014 (2024).
- [28] J. Xu, C. Zhong, S. Zhuang, C. Qian, Y. Jiang, A. Pishe-

- hvar, X. Han, D. Jin, J. M. Jornet, B. Zhen, J. Hu, L. Jiang, and X. Zhang, Slow-wave hybrid magnonics, *Phys. Rev. Lett.* **132**, 116701 (2024).
- [29] Y. Zhao, J. Rao, Y. Gui, Y. Wang, and C.-M. Hu, Broadband nonreciprocity realized by locally controlling the magnon's radiation, *Phys. Rev. Appl.* **14**, 014035 (2020).
- [30] Y. Shi, C. Zhang, C. Jiang, C. K. Ong, and G. Chai, Mirror symmetric nonreciprocity and circular transmission in cavity magnonics, *Appl. Phys. Lett.* **119**, 132403 (2021).
- [31] Y. Yang, J. Rao, Y. Gui, B. Yao, W. Lu, and C.-M. Hu, Control of the magnon-photon level attraction in a planar cavity, *Phys. Rev. Appl.* **11**, 054023 (2019).
- [32] J. W. Rao, Y. P. Wang, Y. Yang, T. Yu, Y. S. Gui, X. L. Fan, D. S. Xue, and C.-M. Hu, Interactions between a magnon mode and a cavity photon mode mediated by traveling photons, *Phys. Rev. B* **101**, 064404 (2020).
- [33] J. Rao, C. Y. Wang, B. Yao, Z. J. Chen, K. X. Zhao, and W. Lu, Meterscale strong coupling between magnons and photons, *Phys. Rev. Lett.* **131**, 106702 (2023).
- [34] H. Huebl, C. W. Zollitsch, J. Lotze, F. Hocke, M. Greifenstein, A. Marx, R. Gross, and S. T. B. Goennenwein, High cooperativity in coupled microwave resonator ferromagnetic insulator hybrids, *Phys. Rev. Lett.* **111**, 127003 (2013).
- [35] L. Bai, M. Harder, Y. P. Chen, X. Fan, J. Q. Xiao, and C.-M. Hu, Spin pumping in electrodynamically coupled magnon-photon systems, *Phys. Rev. Lett.* **114**, 227201 (2015).
- [36] Y. Shi, D. Zhang, C. Zhang, C. Jiang, and G. Chai, Control of photon-magnon coupling with a nonuniform microwave magnetic field, *J. Phys. D: Appl. Phys.* **52**, 305003 (2019).
- [37] Y. Xiong, A. Christy, Y. Dong, A. H. Comstock, D. Sun, Y. Li, J. F. Cahoon, B. Yang, and W. Zhang, Combinatorial split-ring and spiral metaresonator for efficient magnon-photon coupling, *Phys. Rev. Appl.* **21**, 034034 (2024).
- [38] B. Bhoi, B. Kim, J. Kim, Y.-J. Cho, and S.-K. Kim, Robust magnon-photon coupling in a planar-geometry hybrid of inverted split-ring resonator and YIG film, *Sci. Rep.* **7**, 11930 (2017).
- [39] P.-C. Xu, J. W. Rao, Y. Wang, Y. S. Gui, J. Q. Xiao, X. Jin, and C.-M. Hu, Electrical detection of magnon-photon interactions via an auxiliary spin-wave mode, *Phys. Rev. B* **102**, 014453 (2020).
- [40] H. Pan, J. Qian, Z. Rao, C.-M. Hu, and Z. An, Spin pumping of magnons coherently coupled to a cavity dark mode, *Phys. Rev. Appl.* **19**, 014075 (2023).
- [41] S. Guo, D. Russell, J. Lanier, H. Da, P. C. Hammel, and F. Yang, Strong on-chip microwave photon-magnon coupling using ultralow-damping epitaxial $\text{y}_3\text{fe}_5\text{o}_{12}$ films at 2 k, *Nano Lett.* **23**, 5055 (2023).
- [42] A. Ghirri, C. Bonizzoni, M. Maksutoglu, and M. Affronte, Interplay between magnetism and superconductivity in a hybrid magnon-photon bilayer system, *Phys. Rev. Appl.* **22**, 034004 (2024).
- [43] J. T. Hou and L. Liu, Strong coupling between microwave photons and nanomagnet magnons, *Phys. Rev. Lett.* **123**, 107702 (2019).
- [44] Y. Li, T. Polakovic, Y.-L. Wang, J. Xu, S. Lendinez, Z. Zhang, J. Ding, T. Khaire, H. Saglam, R. Divan, J. Pearson, W.-K. Kwok, Z. Xiao, V. Novosad, A. Hoffmann, and W. Zhang, Strong coupling between magnons and microwave photons in on-chip ferromagnet-superconductor thin-film devices, *Phys. Rev. Lett.* **123**, 107701 (2019).
- [45] I. A. Golovchanskiy, N. N. Abramov, V. S. Stolyarov, M. Weides, V. V. Ryazanov, A. A. Golubov, A. V. Ustinov, and M. Y. Kupriyanov, Ultrastrong photon-to-magnon coupling in multilayered heterostructures involving superconducting coherence via ferromagnetic layers, *Sci. Adv.* **7**, eabe8638 (2021).
- [46] H. Maier-Flaig, S. T. B. Goennenwein, R. Ohshima, M. Shiraiishi, R. Gross, H. Huebl, and M. Weiler, Note: Derivative divide, a method for the analysis of broadband ferromagnetic resonance in the frequency domain, *Rev. Sci. Instrum.* **89**, 076101 (2018).
- [47] T. J. Silva, C. S. Lee, T. M. Crawford, and C. T. Rogers, Inductive measurement of ultrafast magnetization dynamics in thin-film permalloy, *J. Appl. Phys.* **85**, 7849 (1999).
- [48] A. Prabhakar and D. D. Stancil, *Spin Waves: Theory and Applications* (Springer US, Boston, MA, 2009).
- [49] J. A. Kong, *Electromagnetic wave theory* (EMW Publishing, Cambridge, MA, 2000).
- [50] A. V. Chumak, A. A. Serga, and B. Hillebrands, Magnon transistor for all-magnon data processing, *Nat. Commun.* **5**, 4700 (2014).
- [51] P. Chen, H. Wang, C. Cheng, C. Wan, D. Zhang, Y. Wang, Y. Wang, W. He, B. Chi, Y. Liu, G. Yu, H. Yu, and X. Han, Complementary magnon transistors by comb-shaped gating currents, *Phys. Rev. Appl.* **20**, 054019 (2023).
- [52] X. Ge, R. Verba, P. Pirro, A. V. Chumak, and Q. Wang, Nanoscaled magnon transistor based on stimulated three-magnon splitting, *Appl. Phys. Lett.* **124**, 122413 (2024).
- [53] Y. Z. Wang, T. Y. Zhang, J. Dong, P. Chen, G. Q. Yu, C. H. Wan, and X. F. Han, Voltage-controlled magnon transistor via tuning interfacial exchange coupling, *Phys. Rev. Lett.* **132**, 076701 (2024).
- [54] T. Schneider, A. A. Serga, B. Leven, B. Hillebrands, R. L. Stamps, and M. P. Kostylev, Realization of spin-wave logic gates, *Appl. Phys. Lett.* **92**, 022505 (2008).
- [55] T. Fischer, M. Kewenig, D. A. Bozhko, A. A. Serga, I. I. Syvorotka, F. Ciubotaru, C. Adelman, B. Hillebrands, and A. V. Chumak, Experimental prototype of a spin-wave majority gate, *Appl. Phys. Lett.* **110**, 152401 (2017).
- [56] Á. Papp, W. Porod, and G. Csaba, Nanoscale neural network using non-linear spin-wave interference, *Nat. Commun.* **12**, 6422 (2021).
- [57] Q. Wang, R. Verba, K. Davidková, B. Heinz, S. Tian, Y. Rao, M. Guo, X. Guo, C. Dubs, P. Pirro, and A. V. Chumak, All-magnonic repeater based on bistability, *Nat. Commun.* **15**, 7577 (2024).